Band Excitations in $CePd_3$: A Comparison of Neutron Scattering and *ab initio* Theory

Eugene A. Goremychkin,[1] Hyowon Park,[2,3] Raymond Osborn,[2,*] Stephan Rosenkranz,[2] John-Paul Castellan,[4] Victor R. Fanelli,[5] Andrew D. Christianson,[6] Matthew B. Stone,[6] Eric D. Bauer,[7] Kenneth J. McClellan,[7] Darrin D. Byler,[7] and Jon M. Lawrence[7,8]

[1] *Frank Laboratory of Neutron Physics, Joint Institute for Nuclear Research, Dubna, Moscow Region, 141980, Russia*
[2] *Materials Science Division, Argonne National Laboratory, Argonne, IL 60439-4845, USA*
[3] *Department of Physics, University of Illinois at Chicago, Chicago, IL 60607, USA*
[4] *Institute for Solid State Physics, Karlsruhe Institute of Technology, D-76021 Karlsruhe, Germany*
[5] *Instrument and Source Division, Oak Ridge National Laboratory, Oak Ridge, TN 37831, USA*
[6] *Quantum Condensed Matter Division, Oak Ridge National Laboratory, Oak Ridge, TN 37831, USA*
[7] *Los Alamos National Laboratory, Los Alamos, NM 87545, USA*
[8] *Department of Physics and Astronomy, University of California, Irvine, CA 92697, USA*

(Dated: February 18, 2022)

Intermediate valence compounds containing rare earth or actinide ions are archetypal systems for the investigation of strong electron correlations. Their effective electron masses of 10 to 50 times the free electron mass result from a hybridization of the highly localized f-electrons with the more itinerant d-electrons, which is strong enough that their properties are dominated by on-site electron correlations. To a remarkable degree, this can be modeled by the Anderson Impurity Model, even though the f-electrons are situated on a periodic lattice. However, in recent years, there has been increasing evidence that the dynamic magnetic susceptibility of intermediate valence compounds is not purely local, but shows variations across the Brillouin zone that have been ascribed to f-band coherence. So far, this has been based on simplified qualitative models. In this article, we present a quantitative comparison of inelastic neutron scattering from a single crystal of $CePd_3$, measured in four-dimensional ($\mathbf{Q}$,ω)-space, with *ab initio* calculations, which are in excellent agreement on an absolute scale. Our results establish that the $\mathbf{Q}$-dependence of the scattering is caused by particle-hole excitations within f-d hybridized bands that grow in coherence with decreasing temperature.

INTRODUCTION

The advent of pulsed neutron sources, which have an enhanced flux of high energy epithermal neutrons, stimulated interest over thirty years ago in the possibility of using inelastic neutron scattering to study single-electron band structures [1, 2]. The neutron cross section, or scattering law, $S(\mathbf{Q},\omega)$, is proportional to the dynamic magnetic susceptibility, $\chi''(\mathbf{Q},\omega)$, of the band electrons [3]. For non-interacting electrons, this is derived from the familiar Lindhard susceptibility, whose imaginary part is proportional to the joint density-of-states of the single-electron bands, $\chi_0''(\mathbf{Q},\omega) \propto \sum_{\mathbf{k}} f_{\mathbf{k}+\mathbf{Q}}(1-f_{\mathbf{k}})\delta(E_{\mathbf{k}+\mathbf{Q}} - E_{\mathbf{k}} - \omega)$. The resulting scattering intensity would be enhanced at momentum transfers, $\mathbf{Q}$, and energy transfers, ω, that connect regions of high densities-of-state in the single-electron bands, $E_{\mathbf{k}}$, whose states are occupied with probability $f_{\mathbf{k}}$, so that neutrons could become a complementary probe of the electronic structure to Angle Resolved Photoemission Spectroscopy (ARPES).

The earliest estimates of the neutron cross section for weakly correlated electron bands were discouraging, with signals in the range 10^{-4} to 10^{-3} barns/steradians/eV spread over wave vectors covering the entire Brillouin zone and energies up to the band width [1]. Such broad distributions of intensity have been challenging to measure at the pulsed neutron time-of-flight spectrometers, where measurements are typically made using a fixed sample geometry. Consequently, such high-energy spectrometers have mostly been used to measure coherent excitations, such as spin waves in the copper oxide and iron-based superconductors [4, 5]. These also represent the magnetic excitations of band electrons, but they are easier to measure because strong interatomic exchange interactions generate poles in the dynamic susceptibility that yield well-defined peaks in the cross section.

Although measuring the electronic structure of weakly correlated electrons may not be technically feasible with neutrons, there has been increasing evidence over the past decade that strongly correlated electron systems, such as the rare earth intermediate valence compounds, show variations in $\chi''(\mathbf{Q},\omega)$ that could result from coherent fermionic bands [6]. Before this, it was generally assumed that the strong correlations in these materials were purely local, confined to f-electron interactions within each ion, so that the electronic excitations of the f-shell were entirely incoherent [7]. However, downturns in the resistivity at low temperature were interpreted as evidence of a growing coherence of strongly renormalized f-bands whose electrons are hybridized with the more itinerant d-electrons [8], an interpretation that was reinforced by evidence of a $\mathbf{Q}$-dependence of the scattering in single crystals of materials such as $CePd_3$ [9], $YbAl_3$ [10] and $CeInSn_2$ [11]. So far, these interpretations have been qualitative, based on conceptual models of $f-d$

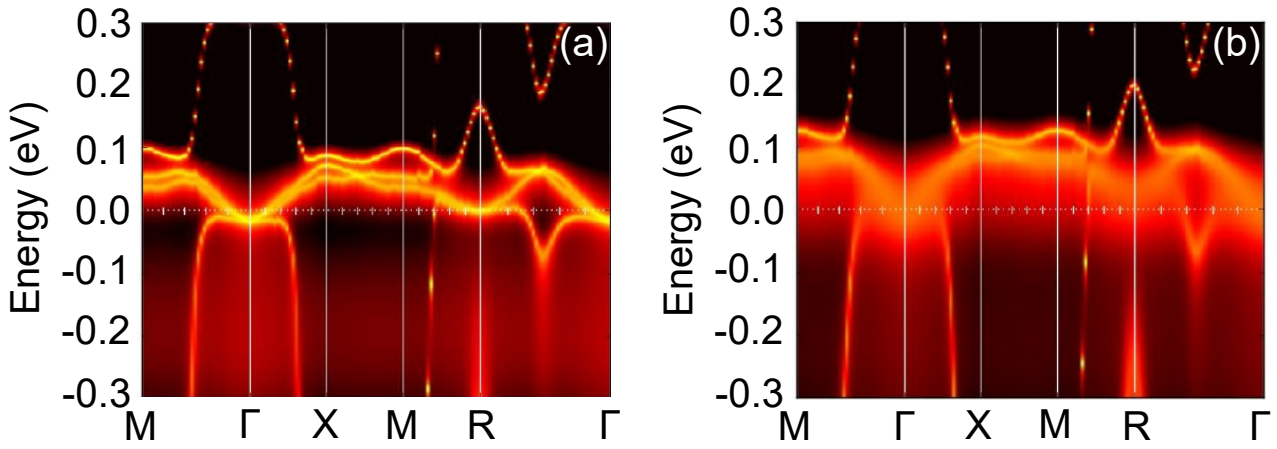

FIG. 1. Electronic spectral function of $CePd_3$ at (a) 100 K and (b) 400 K, calculated by using DFT+DMFT. At low temperature, the calculations show the presence of well-defined quasiparticle bands that cross the Fermi energy producing small electron pockets close to the centre of the Brillouin zone (Γ) and the ($\frac{1}{2}\frac{1}{2}\frac{1}{2}$) zone boundary (R). Flat unoccupied bands near 50 meV are seen at the X-point ($\frac{1}{2}00$) and the M-point ($\frac{1}{2}\frac{1}{2}0$). At 400 K, the spectral weight close to the Fermi energy is largely incoherent.

hybridized bands, because it was not possible to do a quantitative comparison with realistic theories within the experimental limitations of fixed-geometry neutron measurements.

Two recent developments allow us to go beyond the previous qualitative analysis and do a comprehensive quantitative comparison of experiment and theory. The first of these are theoretical advances in the calculation of electronic excitations in strongly correlated electron systems, combining Density Functional Theory (DFT) with Dynamical Mean Field Theory (DMFT), to produce *ab initio* calculations of the dynamic susceptibility that include both single-particle and two-particle vertex corrections, allowing the treatment of systems with both coherent quasiparticles and incoherent spectral weight [12]. We recently drew attention to the qualitative consistency of our earlier neutron scattering data with strongly renormalized band calculations in $CePd_3$ [9, 13], but we have now performed a complete calculation of $S(\mathbf{Q},\omega)$ over the entire Brillouin zone with cross sections placed on an absolute scale.

The second development is the advent of a new generation of inelastic neutron scattering spectrometers with large position sensitive detectors [14, 15] that allow efficient measurements of four dimensional $S(\mathbf{Q},\omega)$ in single crystals by rotating the sample during the data collection. This can be accomplished either by measuring at discrete steps of the rotation angle, which is known as the Horace mode, named after the analysis software developed by R. Ewings and T. G. Perring [16], or by collecting the data continuously as the sample rotates, which is known as the Sweep mode [17]. Both methods produce equivalent results that overcome the limitations of fixed-geometry measurements by measuring entire volumes of $(\mathbf{Q},\omega)$-space rather than a sparse set of hypersurfaces through that volume. Since the experimental data can also be placed on an absolute scale by normalizing the intensity to a vanadium standard, it is possible to produce a parameter-free comparison of experiment and theory.

In this article, we present the results of such a comparison between neutron measurements obtained at the ISIS Pulsed Neutron Source and the Spallation Neutron Source, collected by the Horace and Sweep modes, respectively, and DFT+DMFT calculations. As expected, the calculations show broad distributions of intensity with diffuse maxima at high symmetry points that shift within the Brillouin zone as a function of energy transfer. These match the measured distributions of the dynamic susceptibility with absolute cross sections that are within 20% of the theoretical predictions. Peaks in the dynamic susceptibility at fixed momentum transfer are associated with values of $\mathbf{Q}$ and ω that connect relatively flat regions of the coherent quasiparticle bands, although incoherent scattering processes significantly enhance the overall intensity. The consistency between theory and experiment shows that the DFT+DMFT method provides a highly accurate prediction of the electronic properties in materials with extremely strong electron correlations.

THEORY

The dynamic susceptibility of $CePd_3$ was derived from a calculation of the one-electron Green's function, using density functional theory in combination with dynami-

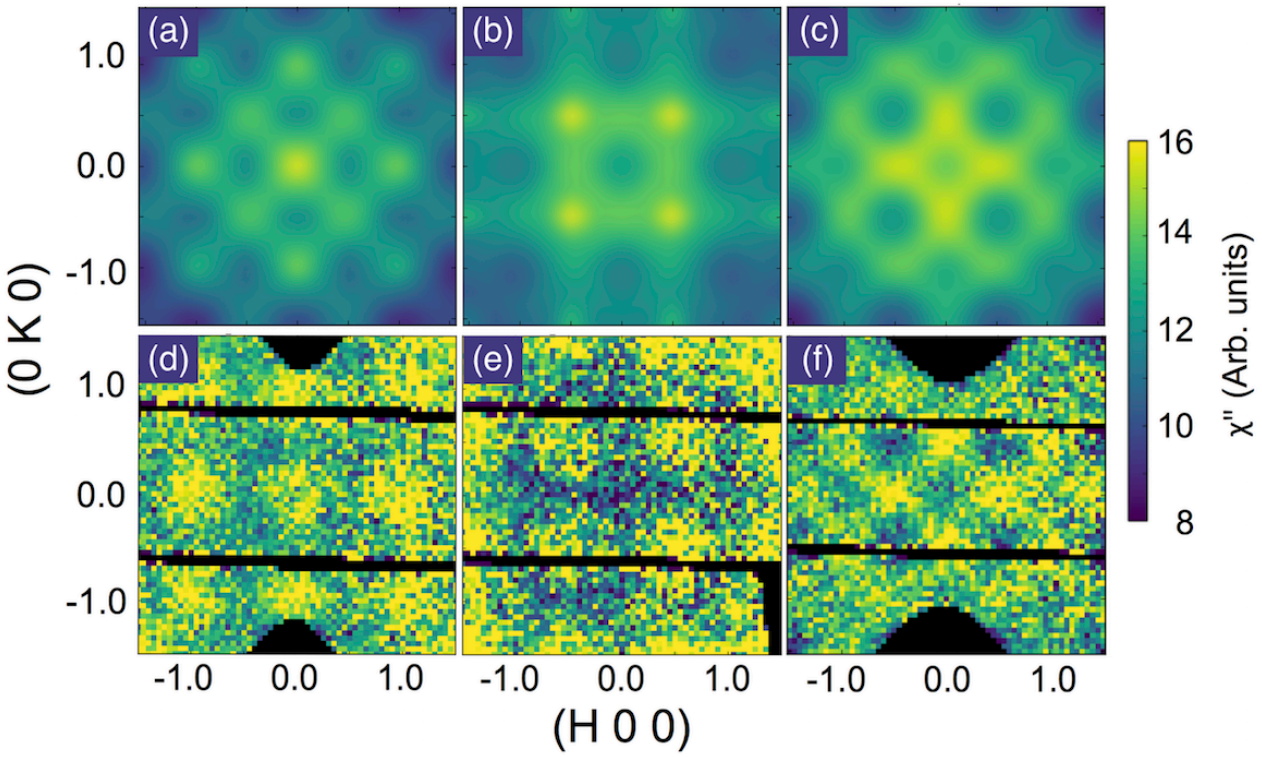

FIG. 2. Dynamic magnetic susceptibility of $CePd_3$ at 100 K (a,b,c) calculated by using DFT+DMFT and (d,e,f) measured by inelastic neutron scattering on ARCS. The results are shown as [H00]/[0K0] planes at constant energy transfers of (a,b,d,e) 35 meV and (c,f) 55 meV, with (a,d) L=1 and (b,c,e,f) L=$\frac{3}{2}$. In both the calculations and measurements, the results are averaged over $\omega = \pm 5$ meV and $L \approx \pm 0.2$. The intensity is in arbitrary units with the calculations and measurements normalized by a single scale factor. No backgrounds have been subtracted from the ARCS data. Black pixels represent regions of reciprocal space that were not measured.

cal mean field theory (DFT+DMFT). This approach allows the incorporation of local correlations, *i.e.* Hund's rule and spin-orbit coupling as well as on-site Kondo screening, into realistic band structures based on DFT. Figure 1 shows the spectral function $A(\mathbf{k},\omega)$, which includes the the one-particle vertex correction, *i.e.*, the electron self-energy. At 100 K, the band structure shows strongly renormalized but well-defined quasiparticle excitations within f-electron bands that are hybridized with the more dispersive d-bands. There are two small Fermi surface pockets centred at the Γ, *i.e.*, $\mathbf{Q}$ =(000), and R-points, *i.e.*, $\mathbf{Q} = (\frac{1}{2}\frac{1}{2}\frac{1}{2})$. Because of the strong spin-orbit coupling, the f-bands have contributions from both $j = \frac{5}{2}$ and $\frac{7}{2}$ states, with the former spread over approximately 100 meV around the Fermi level and the latter at a few hundred meV above the Fermi energy (not shown in Fig. 1). The spin-orbit coupling is also evident in weak incoherent spectral weight at about 200 meV below the Fermi energy. At 400 K, the overall dispersion of the quasiparticles is very similar, but there is a strong increase in the self energy, with a strong reduction of the coherent quasiparticle spectral weight, particularly close to the Fermi energy. We will discuss this later when presenting the high-temperature neutron scattering results.

The dynamic magnetic susceptibility, $\chi''(\mathbf{Q},\omega)$, is computed from the polarization bubble of the fully interacting DFT+DMFT one-particle Green's function, whose spectral weight is shown in Figure 1, by incorporating two-particle irreducible vertex corrections, Γ^{irr}_{loc}, which are assumed to be local in the same basis in which the DMFT self-energy is local [18, 19]. Further details are given in the Supplementary Information.

The calculations generate scattering throughout the Brillouin zone with broad maxima at high symmetry points in $\mathbf{Q}$, which shift with energy transfer. Figure 2 shows $\mathbf{Q} = [H, K]$ scattering planes with $L = 0$ and $L = \frac{1}{2}$ at energy transfers of 35 meV and 55 meV. The calculations are displayed in an extended zone scheme with corrections for the f-electron magnetic form factor. These show that there are maxima in the intensity at the Γ and R-points at $\omega = 35$ meV, but at the M and X points at $\omega = 57$ meV. These maxima are not connected by dispersive modes. Instead, the dynamic susceptibility is peaked at $\sim$ 35 meV and $\sim$ 57 meV in different re-

gions of the Brillouin zone. This is illustrated in Figure 3, which shows slices in the $L-\omega$ plane centred at the X and M-points. The scattering consists of columns of intensity with maxima at the two discrete values of energy transfer.

EXPERIMENT

Using a large single crystal of $CePd_3$, we have performed measurements of four-dimensional S(**Q**,ω) by rotating the sample at fixed incident energies on time-of-flight spectrometers, MERLIN and ARCS, at the ISIS Pulsed Neutron Facility and Spallation Neutron Source, respectively [14, 15]. These possess large banks of position-sensitive detectors that allow the scattered neutrons to be counted as a function of polar and azimuthal angle, with respect to the incident beam. When combined with the sample rotation angle and the neutron time-of-flight, this four-coordinate scattering geometry can be readily transformed into three-dimensional reciprocal space coordinates, **Q**, and a fourth energy coordinate, ω. The transformed data fill large volumes of (**Q**,ω), allowing arbitrary cuts to be made at constant energy or momentum transfer (Fig. 2 and 3). Correction for the temperature factor and calibration to a vanadium standard allows the dynamic magnetic susceptibility to be directly compared to the DFT+DMFT calculations. Uncertainties in the absorption correction mean that there is 20% uncertainty in the cross section.

Figure 4 shows the measured and calculated energy dependence of the scattering at four points in the Brillouin zone. The excellent agreement between the two without adjusting any of the theoretical parameters shows that

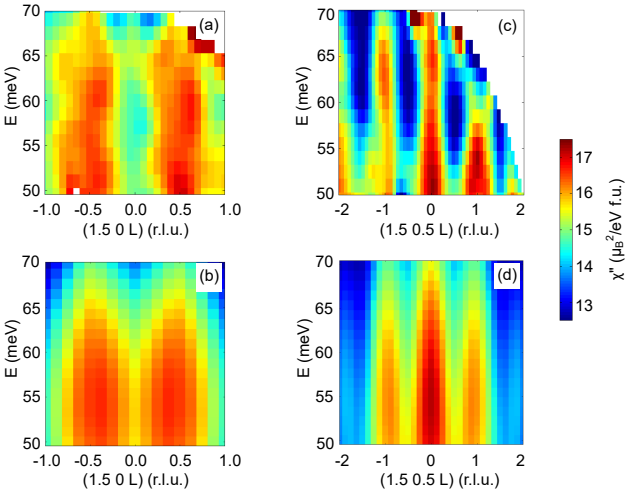

FIG. 3. Dynamic magnetic susceptibility of $CePd_3$ at 5 K ((a), (c) MERLIN data) and the DFT+DMFT calculations at 100 K (b), (d) represented by a L-ω slice at H = (1.5±0.25) and (a,b) K = (0.00±0.25) and and (c,d) K= (0.50±0.25).

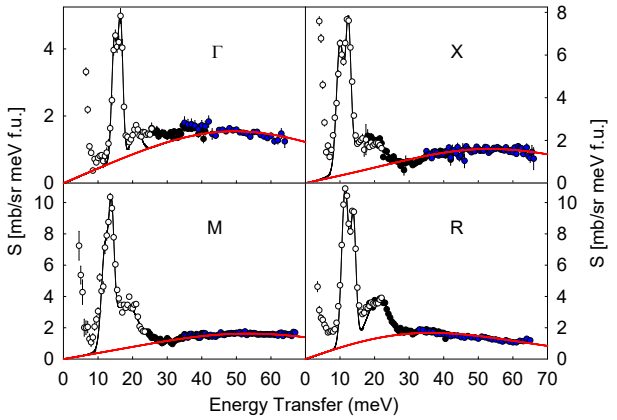

FIG. 4. Energy dependence of the scattering law of $CePd_3$ at 5 K at the Γ (1.00±0.25, 1.00±0.25, 0.00±0.25), X (1.00±0.25, 1.00±0.25, 0.50±0.25), M (1.50±0.25, 0.00±0.25, 0.50±0.25) and R (1.50±0.25, 0.50±0.25, 0.50±0.25) points in the Brillouin zone. The open circles, closed black circles, and closed blue circles are measurements on MERLIN with incident energies of 30 meV, 60 meV, and 120 meV, respectively. The solid black lines show the estimated phonon scattering based on a fit to three Gaussians. The energies of the phonon peaks are in a good agreement with previous measurements of the $CePd_3$ phonons [20]. The red lines are the result of the DFT+DMFT calculations.

the DFT+DMFT calculations accurately reproduces the energy scale for the magnetic fluctuations. The shift in the energy maximum from 35 meV at the Γ and R-points to 57 meV at the M and X-points is evident in the data. The energy dependence of the scattering is also compared to the calculations in Figure 3.

Figure 2 shows the **Q**-dependence derived from experiment, confirming the theoretically predicted shift in the maxima between the Γ and R-points at 35 meV to the M and X-points at 57 meV. The magnetic scattering is superposed on a Q-dependent background from the sample environment, which increases monotonically with momentum transfer, shifting the maxima away from $Q = 0$.

To provide a more quantitative comparison, we show constant energy cuts along a number of high symmetry directions in Figure 5, where the data are plotted against the theoretical calculations on an absolute scale. The instrumental background, which is produced by scattering off the sample environment, is well-described by a quadratic function in Q, so the data have been fitted to the calculated values added to this background. Small adjustments to the overall scale factor of the calculated dynamic susceptibility were included in the fits, but these amounted to less than 20%, which is consistent with the absorption correction from the irregularly shaped sample. Details of these fits are given in the Supplementary Information. The excellent agreement confirms the qualitative consistency of experiment and theory evident in

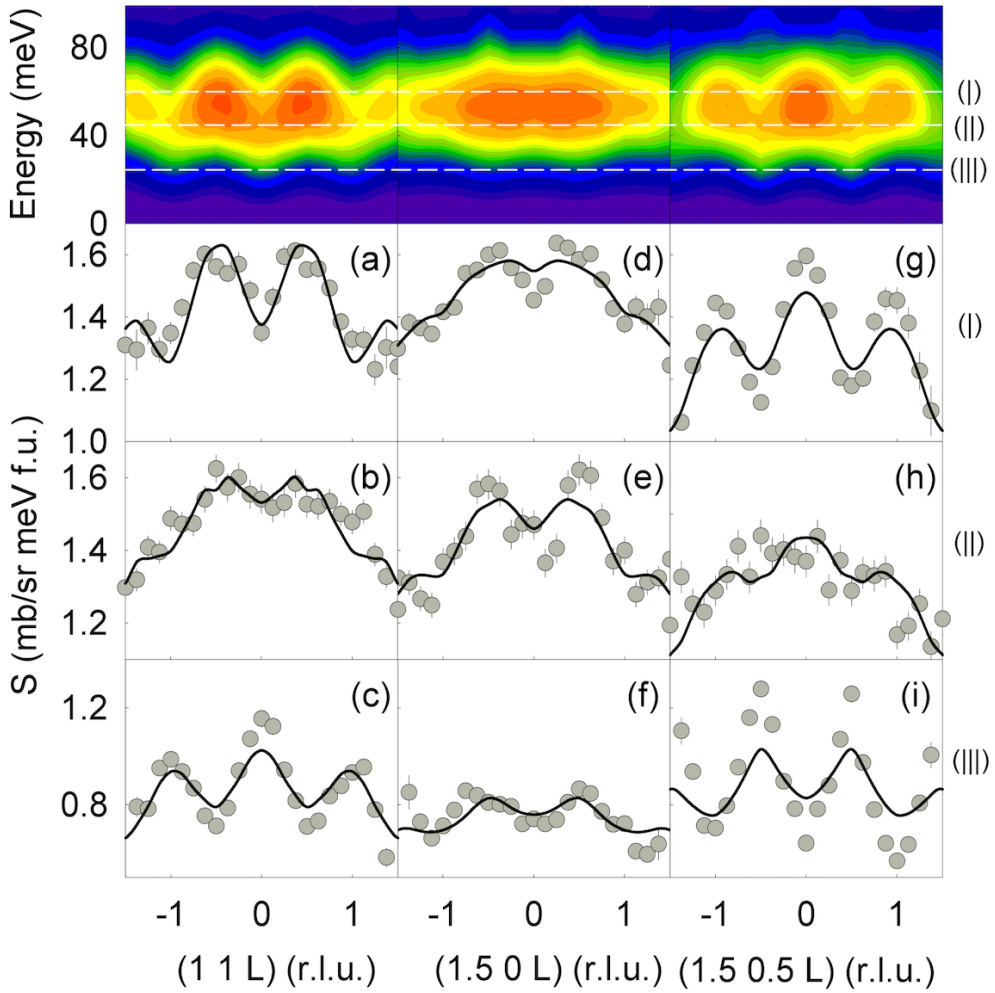

FIG. 5. The upper three panels represent the DFT+DMFT calculations of S($\mathbf{Q}, \omega$) at 100 K in the form of a L-ω slice along $\Gamma \rightarrow$X at H=(1.00±0.25), K=(1.00±0.25), X→M at H=(1.50±0.25), K=(0.00±0.25) and M→R directions at H=(1.50±0.25), K=(0.50±0.25). Three white dashed lines, labelled I, II and III, show the direction and position in energy of the one dimensional constant energy cuts at energies of (a,d,g) 60±5 meV (b,e,h) 45.0±2.5 meV and (c,f,i) 25.0±2.5 meV, respectively. The points represent the inelastic neutron scattering data measured on MERLIN and integrated in the same energy and H, K range as in the upper three panels. The error bars are derived using Poisson statistics. The lines represent one-dimensional cuts of the DFT+DMFT calculations, which have been fit to the data with a single scale factor and quadratic backgrounds as the only adjustable parameters. In the plots, the backgrounds have been subtracted but the data and fits without the background subtraction are shown in the Supplementary Information.

Figures 2 and 3.

Finally, we compare the calculations made at higher temperature to the experimental data. Figure 6 shows that the Q-dependence of the magnetic scattering is almost entirely suppressed at room temperature, which is well above the coherence temperature inferred from transport measurements. This is also predicted by the theoretical calculations. An inspection of the spectral functions at 100 K and 400 K in Figure 1 shows that this results from the substantial reduction in coherence of the one-electron quasiparticles, and confirms the importance of this coherence in generating the observed Q-variations in the dynamic susceptibility at low temperature.

DISCUSSION AND CONCLUSION

Our results demonstrate that it is now possible to determine the electronic structure of intermediate valence materials with considerable accuracy by incorporating local correlations into band structures through the combination of density functional theory and dynamical mean

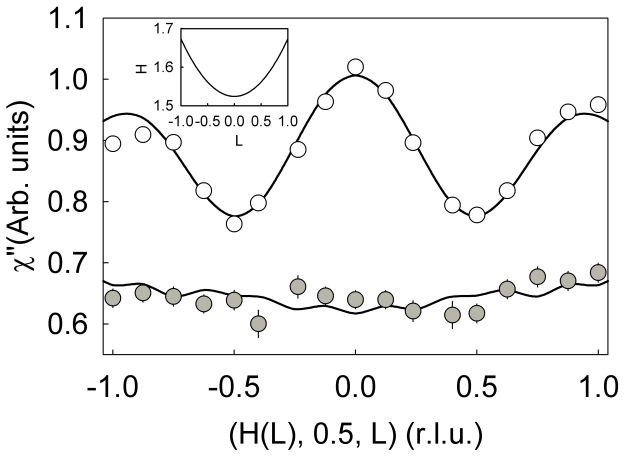

FIG. 6. Temperature dependence of the dynamic magnetic susceptibility measured on the MAPS spectrometer. The open (closed) circles were measured at 6 K (300 K) using a fixed sample geometry (See Ref. 9 for more details) at the energy transfer of (60±10) meV and K = (0.50±0.25). The inset shows how H varies as a function of L. The lines are the results of DFT+DMFT calculations performed at 100 K and 400 K including the H(L) dependence and scaled with the same normalization factor for both temperatures.

field theory. The agreement of the calculated and measured neutron cross sections is complete throughout the Brillouin zone and extending over a broad range of energy transfers. This also shows that inelastic neutron scattering can be used to measure the dynamic susceptibility arising from correlated electron bands without the presence of collective excitations, such as spin waves or crystal field excitons.

In the Supplementary Information, we compare the calculated magnetic response both with and without the two-particle vertex correction, Γ^{irr}_{loc}, which represents the interactions between the electron and the hole excited by the neutron. The correction has two effects: firstly, it smooths out some of the fine structure in the energy dependence of the spectra while broadly preserving both the **Q**-variation and the overall energy scale, and secondly, it produces a strong energy-dependent enhancement of the intensity, for example by a factor of ∼6 at ω = 60 meV (Fig. S4 in the Supplementary Information). Both coherent and incoherent processes therefore make important contributions to the scattering; the **Q**-dependence is determined primarily by the former whereas the energy dependence and the overall intensity are determined primarily by the latter.

In Ref. 9, we showed that the Anderson *Impurity* Model (AIM) is successful in explaining a number of important properties (the magnetic susceptibility $\chi(T)$, the $4f$-occupation number $n_f(T)$, the $4f$ contribution to the specific heat $C_{4f}(T)$, and the **Q**-averaged dynamic susceptibility $\chi''(\omega)$) of intermediate valence compounds such as $CePd_3$, even though the cerium atoms are not impurities but sit on a periodic lattice. We speculated that the reason the impurity model works so well for these periodic systems is that the strong inelastic scattering of the electronic quasiparticles broadens the spectral functions. The first three properties just mentioned are primarily sensitive to the fourth, *i.e.*, $\chi''(\omega)$, which represents *local* $4f$ moment fluctuations. The DFT+DMFT calculations show that the vertex corrections do indeed result in spectra that, when averaged in **Q**, are very similar to the AIM result of Ref. 9, thus helping explain why the impurity model works as well as it does. These inelastic processes are also responsible for the very rapid loss of coherence with temperature; as shown in Figure 6 and in Ref. 9, the spectrum of $CePd_3$ is nearly **Q**-independent at room temperature, and has the quasielastic spectral shape expected for an Anderson impurity.

The results of this comparison between theory and experiment provide significantly new insight into the nature of the correlations in intermediate valence systems. The magnetic fluctuations show a much richer structure than was implied by earlier toy models of hybridized bands, and there is a complex interplay between coherent and incoherent contributions to the electronic spectra that is reflected in the evolution of the dynamic magnetic susceptibility with temperature. The transition from coherent f-electron bands to local moment physics, so long postulated in models of heavy fermion and intermediate valence systems, is seen to be accurately modeled by the latest advances in the *ab initio* theories of correlated electron systems.

METHODS

Synthesis

The single crystal of $CePd_3$ was grown using a modified Czochralski method. A polycrystalline charge was melted on a water-cooled, copper hearth in a tri-arc furnace under an argon atmosphere. The cooled hearth kept the molten charge contained within a solid skin of itself to avoid contamination of the melt. A seed crystal mounted on a water-cooled rod was dipped into the molten compound and pulled upwards while being rotated. By controlling the temperature, the rate of pulling, and the speed of rotation, a single-crystalline cylindrical ingot of 0.5 cm diameter and 5 cm long, with a mass of 17.72 g was produced. The sample was aligned with a [1,0,0] direction held vertical.

Inelastic Neutron Scattering

Inelastic neutron scattering measurements were carried out using the MERLIN and MAPS spectrometers at the

ISIS neutron scattering facility and the ARCS spectrometer at the Spallation Neutron Source. The measurements on MERLIN were performed at 5 K using incident energies of 30 meV, 60 meV and 120 meV. In these measurements, the crystal was mounted with [100] direction vertical and angle ϕ between the incident wavevector, k_i and the [010] direction was rotated in discrete steps of 2° (Horace mode). The data were analyzed using the Horace software application [16]. The ARCS measurements were performed using an incident energy of 120 meV using the so-called Sweep mode, where ϕ was rotated continuously and neutron counts were collected as time-stamped events that were synchronized with the sample rotation angle. The data were analyzed using the Mantid framework [21]. The MAPS experiment was performed at fixed $\phi = 0$, *i.e.*, $k_i \| [010]$ at 7 K and 300 K.

Theory

We performed the charge self-consistent DFT+DMFT calculation and computed the magnetic susceptibility of $CePd_3$ using the Wien2k+DMFT package [22]. The DFT equation was solved using the full potential linearized augmented plane-wave method with the Perdue-Burke-Ernzerhof exchange-correlation functional as implemented in the Wien2k code [23]. The quantum impurity problem within DMFT was solved using the continuous-time quantum Monte Carlo (CTQMC) method [24, 25]. We set the on-site Coulomb interaction $U = 6$ eV and the Hund's coupling $J = 0.7$ eV, as previously used for elemental Ce in the α and γ phases [26]. We set the lattice constant of the $CePd_3$ cubic unit cell to 4.126Å, as measured in experiment. More details are given in the Supplementary Information.

* rosborn@anl.gov

[1] Sinha, S. K., Cooke, J. F. & Murani, A. P. Proceedings of the 1984 Workshop on High-Energy Excitations in Condensed Matter. Tech. Rep., Los Alamos National Laboratory (1984).

[2] Cooke, J. F. & Blackman, J. A. Calculation of neutron cross sections for interband transitions in semiconductors. *Physical Review B* **26**, 4410–4420 (1982).

[3] Balcar, E. & Lovesey, S. W. *Theory of Magnetic Neutron and Photon Scattering* (Clarendon Press, 1989).

[4] Coldea, R. *et al.* Spin Waves and Electronic Interactions in La_2CuO_4. *Physical Review Letters* **86**, 5377–5380 (2001).

[5] Dai, P. Antiferromagnetic order and spin dynamics in iron-based superconductors. *Reviews of Modern Physics* **87**, 855–896 (2015).

[6] Riseborough, P. S. & Lawrence, J. M. Mixed valent metals. *Reports on Progress in Physics* **79**, 084501 (2016).

[7] Holland-Moritz, E., Loewenhaupt, M., Schmatz, W. & Wohlleben, D. K. Spontaneous Relaxation of the Local 4f Magnetization in $CePd_3$. *Physical Review Letters* **38**, 983–986 (1977).

[8] Lawrence, J. M., Thompson, J. D. & Chen, Y. Y. Two Energy Scales in $CePd_3$. *Physical Review Letters* **54**, 2537–2540 (1985).

[9] Fanelli, V. R. *et al.* Q-dependence of the spin fluctuations in the intermediate valence compound $CePd_3$. *Journal of Physics: Condensed Matter* **26**, 225602 (2014).

[10] Christianson, A. D. *et al.* Localized Excitation in the Hybridization Gap in $YbAl_3$. *Physical Review Letters* **96**, 117206 (2006).

[11] Murani, A. P., Severing, A., Enderle, M., Steffens, P. & Richard, D. Possible Anisotropic s−f Hybridization in a Cubic Heavy-Fermion Compound: $CeIn_1Sn_2$. *Physical Review Letters* **101**, 206405 (2008).

[12] Kotliar, G. *et al.* Electronic structure calculations with dynamical mean-field theory. *Reviews of Modern Physics* **78**, 865–951 (2006).

[13] Sakai, O. Band Calculations for Ce Compounds with $AuCu_3$-type Crystal Structure on the basis of Dynamical Mean Field Theory: I. $CePd_3$ and $CeRh_3$. *Journal Of The Physical Society Of Japan* **79**, 114701 (2010).

[14] Bewley, R. I. *et al.* MERLIN, a new high count rate spectrometer at ISIS. *Physica B* **385-386**, 1029–1031 (2006).

[15] Abernathy, D. L. *et al.* Design and operation of the wide angular-range chopper spectrometer ARCS at the Spallation Neutron Source. *Review of Scientific Instruments* **83**, 015114 (2012).

[16] Ewings, R. A. *et al.* Horace: Software for the analysis of data from single crystal spectroscopy experiments at time-of-flight neutron instruments. *Nuclear Instruments & Methods In Physics Research Section A* **834**, 132–142 (2016).

[17] Weber, F. *et al.* Electron-Phonon Coupling in the Conventional Superconductor YNi_2B_2C at High Phonon Energies Studied by Time-of-Flight Neutron Spectroscopy. *Physical Review Letters* **109**, 057001 (2012).

[18] Jarrell, M. Hubbard model in infinite dimensions: A quantum Monte Carlo study. *Physical Review Letters* **69**, 168–171 (1992).

[19] Park, H., Haule, K. & Kotliar, G. Magnetic Excitation Spectra in $BaFe_2As_2$: A Two-Particle Approach within a Combination of the Density Functional Theory and the Dynamical Mean-Field Theory Method. *Physical Review Letters* **107**, 137007 (2011).

[20] Loong, C.-K., Zarestky, J. L., Stassis, C., McMasters, O. D. & Nicklow, B. Lattice dynamics of $CePd_3$. *Physical Review B* **38**, 7365 (1988).

[21] Arnold, O. *et al.* Mantid—Data analysis and visualization package for neutron scattering and μSR experiments. *Nuclear Instruments & Methods A* **764**, 156–166 (2014).

[22] Haule, K., Yee, C.-H. & Kim, K. Dynamical mean-field theory within the full-potential methods: Electronic structure of $CeIrIn_5$, $CeCoIn_5$, and $CeRhIn_5$. *Physical Review B* **81**, 195107 (2010).

[23] Blaha, P., Schwarz, K., Madsen, G. K. H., Kvasnicka, K. *et al. Wien2K* (Karlheinz Schwarz, Technische Universitat Wien, Austria, 2001).

[24] Haule, K. Quantum Monte Carlo impurity solver for cluster dynamical mean-field theory and electronic structure calculations with adjustable cluster base. *Physical Review B* **75**, 155113 (2007).

[25] Werner, P., Comanac, A., de' Medici, L., Troyer, M. & Millis, A. J. Continuous-Time Solver for Quantum Impurity Models. *Physical Review Letters* **97**, 076405 (2006).
[26] Chakrabarti, B., Pezzoli, M. E., Sordi, G., Haule, K. & Kotliar, G. α-γ transition in cerium: Magnetic form factor and dynamic magnetic susceptibility in dynamical mean-field theory. *Physical Review B* **89**, 125113 (2014).

END NOTES

Acknowledgements

The research at the Joint Institute for Nuclear Research was supported by the Russian Foundation for Basic Research project 16-02-01086. The research at Argonne National Laboratory and Los Alamos National Laboratory was supported by the Materials Sciences and Engineering Division, Office of Basic Energy Sciences, U.S. Department of Energy. The research at Oak Ridge National Laboratory's Spallation Neutron Source was supported by the Scientific User Facilities Division, Office of Basic Energy Sciences, U.S. Department of Energy. Neutron experiments were performed at the Spallation Neutron Source, Oak Ridge National Laboratory, USA, and the ISIS Pulsed Neutron Source, Rutherford Appleton Laboratory, UK. We gratefully acknowledge the computing resources provided on Blues, a high-performance computing cluster operated by the Laboratory Computing Resource Center at Argonne National Laboratory. We are also grateful for useful discussions with Peter Riseborough.

Author contributions

The single crystal was grown by E.D.B., K.J.M, and D.D.B. The experiments were devised by J.M.L., E.A.G., V.R.F., A.D.C., S.R, and R.O. The inelastic neutron scattering experiments were performed by J.M.L., E.A.G., V.R.F., A.D.C., J.P.C., S.R, R.O, and. M.B.S. The data were analyzed by E.A.G, J.P.C., S.R., V.R.F. and J.M.L. The theoretical calculations were performed by H.P. The manuscript and supplementary information were written by R.O., E.A.G., J.M.L., and H.P. with input from all the authors.

Supplementary Information

THEORY

DFT+DMFT Method

The *ab initio* calculations of the dynamic magnetic susceptibility combine realistic band structures, calculated using density function theory (DFT), followed by solving the quantum impurity problem within Dynamic Mean Field Theory (DMFT), in order to incorporate strong on-site correlations into the one-particle Green function. This DFT+DMFT approach has proved to be a powerful way of obtaining one-particle spectra that include both coherent quasiparticles and incoherent spectral weight from self-energy corrections [1].

The localized Ce $4f$ orbitals are constructed from a projector function in such a way that the f character is maximized, with self-consistent DFT calculations performed using the Wien2k+DMFT package [2]. The DFT+DMFT equation is solved using the full potential linearized augmented plane-wave method with the Perdue-Burke-Ernzerhof exchange-correlation functional as implemented in the Wien2k code [3]. The quantum impurity problem within DMFT is solved using the continuous-time quantum Monte Carlo (CTQMC) method [4, 5]. We set the on-site Coulomb interaction U=6eV and the Hund's coupling J=0.7eV as previously used for the elemental Ce in α and γ phases [6]. The lattice constant of the $CePd_3$ cubic unit cell used in the calculation is 4.126Å as measured in experiment. The calculated one-particle spectral weight is shown in Fig. S1.

The neutron scattering cross section is proportional to the imaginary part of the magnetic susceptibility, $\chi(\mathbf{q},\omega)$, which is computed using a two-particle vertex method as developed in Ref. 19. $\chi(\mathbf{q}, i\omega_n)$ on the imaginary Matsubara frequency $i\omega_n$ axis can be obtained by summing the two-particle Green's function $\chi(i\nu, i\nu')_{\mathbf{q},i\omega}$ closed by the total magnetic moment vertex ($\mu_J = g_J\mu_B\mathbf{J}$) over fermionic Matsubara frequencies

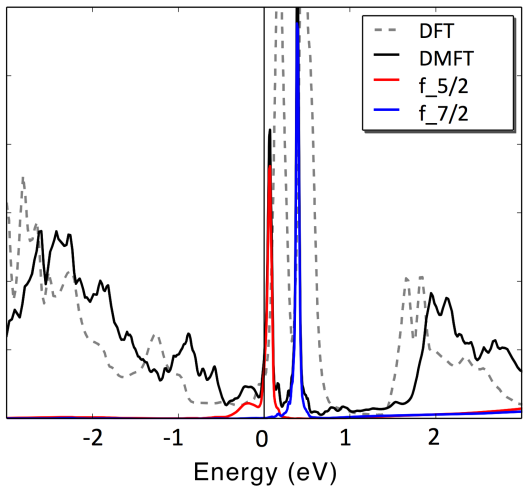

FIG. S1. Spectral weight of $CePd_3$ of the DFT and the DFT+DMFT calculations integrated over the Brillouin zone, showing a decomposition of the f-electron spectra into contributions from different spin-orbit states with $j = \frac{5}{2}$ (red) and $j = \frac{7}{2}$ (blue).

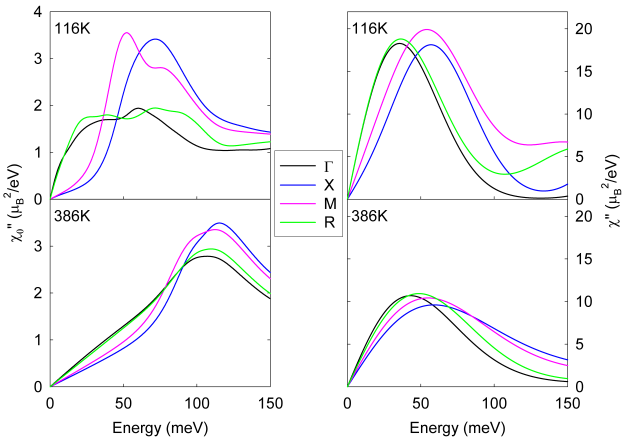

FIG. S3. Calculated susceptibility at four locations in the Brillouin zone using the DFT+DMFT method. The upper and lower panels show calculations at 116 K and 386 K, respectively (left) before and (right) after applying the two-particle vertex correction, Γ^{irr}_{loc}.

$(i\nu, i\nu')$ and magnetic moment indices (α_{1-4}):

$$\chi(\mathbf{q}, i\omega_n) = T \sum_{i\nu, i\nu'} \sum_{\substack{\alpha_1\alpha_2 \\ \alpha_3\alpha_4}} (\mu^z_J)_{\alpha_1\alpha_3} (\mu^z_J)_{\alpha_2\alpha_4} \cdot \chi^{\alpha_1,\alpha_2}_{\alpha_3,\alpha_4}(i\nu, i\nu')_{\mathbf{q},i\omega_n} \cdot \tag{1}$$

$\chi(i\nu, i\nu')_{\mathbf{q},i\omega}$ can be computed by the Bethe-Salpeter equation using the local irreducible vertex function Γ^{irr}_{loc} (Fig. S2):

$$\chi^{\alpha_1,\alpha_2}_{\alpha_3,\alpha_4}(i\nu, i\nu')_{\mathbf{q},i\omega} = [(\chi^0)^{-1}_{\mathbf{q},i\omega} - T \cdot \Gamma^{irr}_{loc}]^{-1}. \tag{2}$$

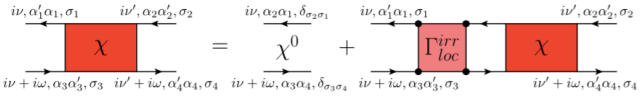

FIG. S2. The Feynman diagrams for the Bethe-Salpeter equation taken from Ref. 19. It relates the two-particle Greens function with the polarization and the local irreducible vertex function (Γ^{irr}_{loc}). The nonlocal two-particle Greens function is obtained by replacing the local propagator by the nonlocal propagator.

Here, the polarization function χ^0 is given as the convolution of the fully interacting one-particle Green's function $G_{\mathbf{k}}$: $\chi^0_{\mathbf{q}} = \frac{1}{N_k}\sum_{\mathbf{k}} G_{\mathbf{k}} \cdot G_{\mathbf{k}+\mathbf{q}}$, and Γ^{irr}_{loc} is obtained by the inverse of the Bethe-Salpeter equation:

$$\Gamma^{irr}_{loc\,\alpha_3,\alpha_4}{}^{\alpha_1,\alpha_2}(i\nu, i\nu')_{i\omega} = \frac{1}{T}[(\chi^0_{loc})^{-1}_{i\omega} - \chi^{-1}_{loc}] \tag{3}$$

where the local two-particle Green's function χ_{loc} is sampled by the CTQMC simulations. Finally, the obtained $\chi(\mathbf{q}, i\omega_n)$ is analytically continued $(i\omega_n \to \omega)$ to the real frequency $\chi(\mathbf{q}, \omega)$ using the maximum entropy method.

Effect of Two-Particle Vertex Correction

In Figure S3, we compare the calculated dynamic magnetic susceptibility before and after including the two-particle vertex correction. Note that this still includes the one-particle vertex correction that generates the quasiparticle broadening seen in Fig. 1 of the main article. However, the additional correction has two main consequences: firstly, some of the fine structure that reflects details of the coherent quasiparticle joint densities-of-state is no longer evident, resulting in much smoother spectra as a function of energy transfer, although the overall energy scales are similar.

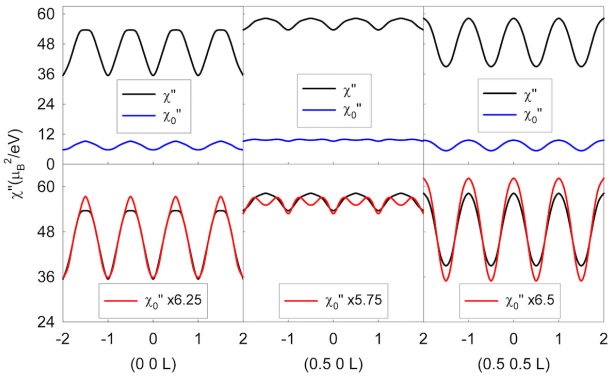

FIG. S4. Calculated susceptibility along three different directions in reciprocal space at an energy transfer of 60 meV. The upper panels show calculations (blue) before and (black) after applying the two-particle vertex correction. The lower panels shows the same calculations after scaling the uncorrected calculations by ∼6.

Secondly, the susceptibility is strongly enhanced by about a factor 6. This is most clearly seen in Fig. S4, where the calculations with and without the two-particle correction are directly compared. This shows that the main effect of the correction is to amplify the signal while preserving the Q-dependence seen in the uncorrected calculations.

EXPERIMENT

Normalization

The DMFT+DFT calculations generate $\chi_{zz}(\mathbf{Q},\omega)$ in units of μ_B^2/meV. For a cubic system such as $CePd_3$, it is possible to derive the instantaneous f-electron moment, using the moment sum rule [8]:

$$\mu_f^2 = 3g_J^2\mu_B^2 \int_{\mathbf{Q}\in BZ}\int_{\omega=-\infty}^{\infty} \frac{\chi''_{zz}(\mathbf{Q},\omega)}{(1-e^{-\omega/kT})} d\mathbf{Q}d\omega \quad (4)$$

The calculations, when integrated up to 20 eV, yield an instantaneous moment of 6.675 μ_B^2 at 5 K, slightly higher than the expected Ce^{3+} moment of 6.429 μ_B^2 by about 4%. Similarly, the static susceptibility can be derived using the Kramers-Kronig relation:

$$\chi_{st} = \frac{1}{\pi}\int_{-\infty}^{\infty} \frac{3g_J^2\chi''_{zz}(\mathbf{Q}\to 0,\omega)}{\omega} d\omega \quad (5)$$

This gives $\chi_{st} = 1.69\times10^{-3}$ emu/mol, which is also slightly higher than the experimental value of 1.4×10^{-3} emu/mol [9] by about 20%. These discrepancies are within the experimental uncertainties in our comparisons with the neutron data, as discussed below.

The experimental data measured on the MERLIN spectrometer at the ISIS Pulsed Neutron Source is in the form of $S(\mathbf{Q},\omega)$, which is placed on an absolute scale after calibration with a standard vanadium sample, using the standard data reduction procedures implemented by the Horace and Mantid software packages [10, 21]. The units

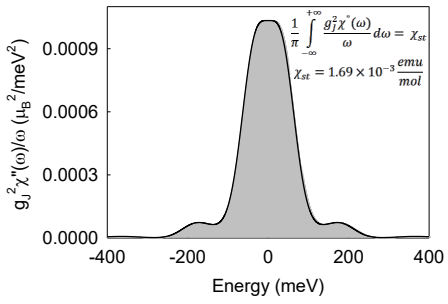

FIG. S5. Energy dependence of the calculated local susceptibility, *i.e.*, integrated over the first Brillouin zone.

shown in figures in the main article can be converted to the calculated units using [12]:

$$S(\mathbf{Q},\omega)[mb/meVsrf.u.]\times 13.77 = 2g_J^2f^2(\mathbf{Q})\chi''_{zz}(\mathbf{Q},\omega)[\mu_B^2/eVf.u.] \quad (6)$$

ignoring the temperature factor, which is approximately 1 for all our measurements. The factor 2 (instead of 3) is because inelastic neutron scattering only measures the two components of the dynamic magnetic susceptibility that are orthogonal to the experimental wavevector (see equation 8 in Ref. 12).

In our comparisons of the DFT+DMFT calculations with the experimental data, we corrected the calculations for the Ce^{3+} form factor using the numerical approximation scheme defined in Ref. 13, as implemented by the Python package, *periodictable* (http://periodictable.readthedocs.io/). Because tabulated values for Ce^{3+} are not available, the form factor was approximated by the Pr^{3+} form factor.

Equation 6 shows that we should be able to convert the DFT+DMFT model into the neutron cross section by dividing by $13.77/(2g_J)^2$, *i.e.*, a scale factor of 9.37. As shown in the next section, the fitted value was ∼10.

There is an additional uncertainty due to self-shielding. We are unable to do a reliable quantitative correction for this, but the single crystal was approximately 5 mm thick, which would produce a self-shielding factor of ∼0.82 when perpendicular to the beam, and less at other rotation angles. This would reduce the scale factor from ∼10 to 8 or less. Because of this and uncertainties in the theoretical normalization, we estimate that there is an uncertainty in the quantitative agreement between theory and experiment of ∼20%.

Backgrounds

The backgrounds in the inelastic neutron scattering data arose primarily from single phonon scattering from the sample and the sample environment, which increases quadratically with wavevector transfer, $\mathbf{Q}$, although there were also contributions from multiple scattering. Most of the single phonon scattering occurs below an energy transfer of 25 meV, and the backgrounds are particularly low above 50 meV (see Fig. S6).

The scale factor for normalizing the model calculations to the data was therefore set by fitting the data at an energy transfer of 60 meV to the model plus a quadratic background. This gave a value of the scale factor of ∼10. As the lower panels of Fig. S7 show, the minimum of the estimated quadratic background agrees very well with the background determined from the empty sample holder, so the difference between the blue dashed lines and the empty circles represents backgrounds from the sample itself.

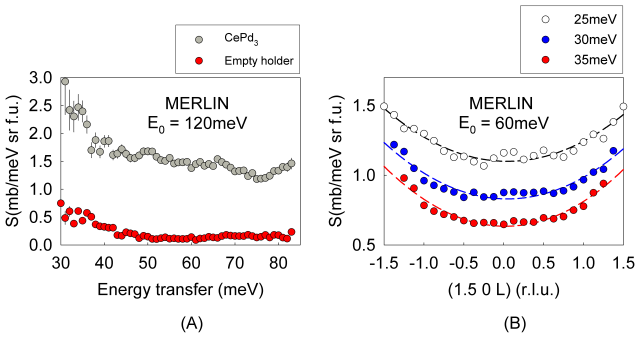

FIG. S6. (A) Comparison of scattering from $CePd_3$ (grey circles) with the empty sample holder (red circles), measured with an incident energy of 120 meV at the Γ point: H = (2.00±0.25) K = (0.00±0.25) L = (0.00±0.25)). (B) Examples of evolution of the background scattering for constant energy cuts measured with E_0 = 60 meV. The dashed lines are quadratic fits to the experimental points.

The same scale factor was then used in fits of the model+quadratic background at other energy transfers. The upper panels of Fig. S7 show the fits at $\omega = 25$ meV. Once again, the minima of the estimated backgrounds agree well with the empty sample holder measurements, giving confidence that this is a valid way of estimating the Q-dependent backgrounds.

Fig. S8 shows the same fits as Fig. 5 of the main article, without subtracting the backgrounds, to help appreciate the influence of the background subtraction on the comparison between theory and experiment.

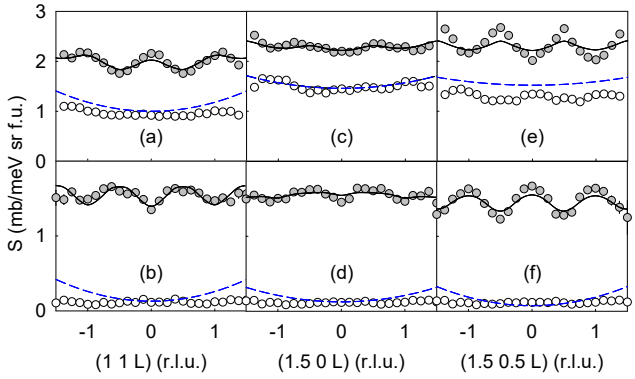

FIG. S7. Fits of the measured data to the DFT+DMFT model at energy transfers of 25 meV (upper panels) and 60 meV (lower panels). The data (filled circles) were fit to the sum of the model, normalized by a single scale factor, and a quadratic background (blue dashed line), giving the black solid line. Data with an empty sample holder measured in the same configuration are shown as open circles.

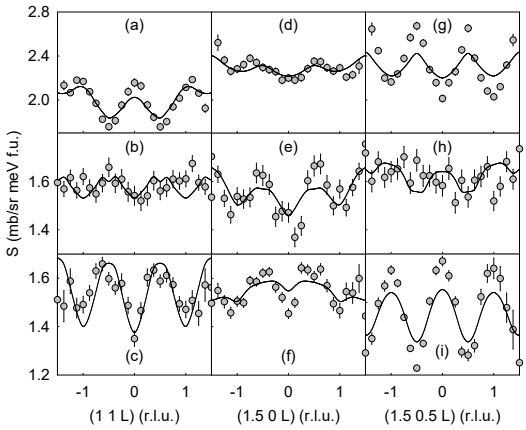

FIG. S8. One dimensional constant energy cuts along the Γ→X at H=(1.00±0.25), K=(1.00±0.25), X→M at H=(1.50±0.25), K=(0.00±0.25) and M→R directions at H=(1.50±0.25), K=(0.50±0.25), at energies of (a,d,g) 25.0±2.5 meV, (b,e,h) 45.0±2.5 meV and (c,f,i) 60±5 meV. The points represent the inelastic neutron scattering measurements integrated in the same energy and H, K ranges. The lines represent one-dimensional cuts of the DFT+DMFT calculations, which have been fit to the data with a single scale factor as the only adjustable parameter. The fits include a background that is quadratic in Q, which has *not* been subtracted from the experimental points (*cf* Fig. 5 in the main article, in which the quadratic backgrounds have been subtracted).

* rosborn@anl.gov

[1] Kotliar, G. *et al.* Electronic structure calculations with dynamical mean-field theory. *Reviews of Modern Physics* **78**, 865–951 (2006).

[2] Haule, K., Yee, C.-H. & Kim, K. Dynamical mean-field theory within the full-potential methods: Electronic structure of $CeIrIn_5$, $CeCoIn_5$, and $CeRhIn_5$. *Physical Review B* **81**, 195107 (2010).

[3] Blaha, P., Schwarz, K., Madsen, G. K. H., Kvasnicka, K. *et al. Wien2K* (Karlheinz Schwarz, Technische Universitat Wien, Austria, 2001).

[4] Haule, K. Quantum Monte Carlo impurity solver for cluster dynamical mean-field theory and electronic structure calculations with adjustable cluster base. *Physical Review B* **75**, 155113 (2007).

[5] Werner, P., Comanac, A., de' Medici, L., Troyer, M. & Millis, A. J. Continuous-Time Solver for Quantum Impurity Models. *Physical Review Letters* **97**, 076405 (2006).

[6] Chakrabarti, B., Pezzoli, M. E., Sordi, G., Haule, K. & Kotliar, G. α-γ transition in cerium: Magnetic form factor and dynamic magnetic susceptibility in dynamical mean-field theory. *Physical Review B* **89**, 125113 (2014).

[7] Park, H., Haule, K. & Kotliar, G. Magnetic Excitation Spectra in $BaFe_2As_2$: A Two-Particle Approach within a Combination of the Density Functional Theory and the Dynamical Mean-Field Theory Method. *Physical Review Letters* **107**, 137007 (2011).

[8] Balcar, E. & Lovesey, S. W. *Theory of Magnetic Neutron and Photon Scattering* (Clarendon Press, 1989).

[9] Kappler, J. P. *et al.* Electronic structure of cerium in $Ce_{1-x}Y_xPd_3$ and $Ce_{1-x}M_xAl_2$ (M = Sc, Y). *Journal of Applied Physics* **53**, 2152–2154 (1982).

[10] Ewings, R. A. *et al.* Horace: Software for the analysis of data from single crystal spectroscopy experiments at time-of-flight neutron instruments. *Nuclear Instruments & Methods In Physics Research Section A* **834**, 132–142 (2016).

[11] Arnold, O. *et al.* Mantid—Data analysis and visualization package for neutron scattering and μSR experiments. *Nuclear Instruments & Methods In Physics Research Section A* **764**, 156–166 (2014).

[12] Xu, G., Xu, Z. & Tranquada, J. M. Absolute cross-section normalization of magnetic neutron scattering data. *Review of Scientific Instruments* **84**, 083906 (2013).

[13] Anderson, I. S. *et al. International Tables for Crystallography*, chap. 4.4, 430–487 (John Wiley & Sons, Ltd, 2006).